

Crystal Phase Mediated Restructuring of Pt on TiO₂ with Tunable Reactivity: Redispersion versus Reshaping

Xiaoben Zhang^{1, 2, 4 †}, Zhimin Li^{2, 4 †}, Wei Pei^{5 †}, Gao Li^{2 *}, Wei Liu¹, Pengfei Du^{1, 4}, Zhen Wang^{1, 5}, Zhaoxian Qin^{2, 4}, Si Zhou^{5 *}, Jijun Zhao⁵, Bing Yang^{1, 3 *}, Wenjie Shen²

¹Dalian National Laboratory for Clean Energy, Dalian Institute of Chemical Physics, Chinese Academy of Sciences, Dalian, 116023, China.

² State Key Laboratory of Catalysis, Dalian Institute of Chemical Physics, Chinese Academy of Sciences, Dalian, 116023, China.

³ CAS Key Laboratory of Science and Technology on Applied Catalysis, Dalian Institute of Chemical Physics, Chinese Academy of Sciences, Dalian, 116023, China.

⁴ University of Chinese Academy of Sciences, Beijing 100049, China.

⁵ Key Laboratory of Materials Modification by Laser, Ion and Electron Beams (Dalian University of Technology), Ministry of Education, Dalian, 116024, China.

†These authors contributed equally.

*e-mail: gaoli@dicp.ac.cn; sizhou@dlut.edu.cn; byang@dicp.ac.cn;

Abstract: Restructuring of supported metal nanoparticles (NPs) e.g., reshaping and redispersion are of tremendous interest for the rational design of high-efficiency catalyst materials with precise particle sizes, shapes, and reactivities. Here we show a crystal phase mediated restructuring of Pt NPs on TiO₂, as a simple approach for fabricating either atomically dispersed single atoms (SAs) or reshaped planar NPs of Pt catalysts with tunable reactivities. Utilizing a variety of state-of-the-art characterizations, we showed that rutile TiO₂ favors the reshaping of 2D planar Pt NPs, whereas the anatase surface facilitates the redispersion of Pt NPs to SAs upon calcination in the air up to 400 °C. Environmental transmission electron microscopy (ETEM) and density function theory (DFT) calculations were employed to directly visualize the dynamic transformation of Pt NPs and reveal the specific role that TiO₂ supports play in promoting the stability and diffusion of Pt SAs. As a result, the reverse reactivity was achieved by tuning their distinct restructuring behaviors. Thus, the Pt SAs on anatase TiO₂ preferentially activated selective hydrogenation of phenylacetylene ($21.22 \times 10^{-2} \text{ s}^{-1}$ at 50 °C), while planar Pt NPs on rutile significantly enhanced the combustion of methane ($3.11 \times 10^{-2} \text{ s}^{-1}$ at 310 °C). Our results therefore open up new routes for tuning the restructuring behavior of supported metal catalysts and designing catalysts with controlled catalytic structures and reactivities.

Introduction

The particle sizes and shapes of metal catalysts are critical in determining their electronic and catalytic properties, ranging from nanosized particles to metal clusters or even single atoms.¹⁻⁴ Supported Pt nanoparticles (NPs), for instance, have been extensively studied due to their extraordinary catalytic performance in a vast variety of catalytic reactions.⁵⁻⁷ Recently, Pt single atom (SA) catalysts have been found to exhibit superior efficiencies by maximizing the use of precious metals.⁸⁻¹¹ However, the specific structure of the active species for a given reaction has not yet been fully explained.¹²⁻¹⁶ Particularly in sub-nanometer range, an effective approach to control the size, shape and thus the reactivity of active metal species is still lacking. Hence, the precise control in the fabrication of Pt NPs/SAs is a crucial step toward designing high-efficiency catalyst materials.

Restructuring of metal NPs on oxide supports has recently attracted tremendous interest for precisely controlling particle size, shape, and composition dynamically in heterogeneous catalysis.¹⁷⁻²² Among these, redispersion is a common route for disintegrating metal NPs into SAs via metal-gas/ligand/support interactions.^{13, 23-25} High-temperature treatment in oxygen, CO, and ligand environments has been widely adopted for the fabrication of Pt, Rh, and other metal SAs on many oxide surfaces.²⁶ Additionally, reshaping has also been intensively investigated as another method for the restructuring of NPs in gas environments. Oxygen, CO, and even inert N₂ can significantly alter the shape of NPs under realistic conditions.^{18, 21} Both metal-gas and metal-support interaction are believed to play a significant role, but the underlying mechanisms and tuning factors are still unclear. As for the metal-support interaction for instance, strong interaction with surface defects is considered to be a key factor for anchoring the as-formed SAs.^{10, 23, 27} while in some circumstances, the reshaped NPs can be also stabilized via strong metal-support interactions (SMSI).²⁸⁻³⁰ However, precisely tuning the restructuring of metal catalysts between the redispersion and reshaping via metal-support interactions has not yet been well depicted, particularly using the same control method with similar metal loading and gas environment.

Herein, we report a crystal phase mediated restructuring (redispersion/reshaping) of Pt catalysts on TiO₂ as a simple approach to precisely tuning their restructuring behaviors and reactivity. Approximately 1 nm Pt NPs were pre-synthesized and impregnated onto anatase and rutile TiO₂. After calcination at 400°C in the air, we clearly identified crystal phase mediated restructuring of Pt NPs on TiO₂, which formed either planar Pt NPs or atomically dispersed Pt SAs, as evidenced by ex situ and in situ scanning transmission electron microscopy (STEM), Fourier transformed infrared spectroscopy (FTIR), and temperature-programmed reduction (TPR) analysis. Density functional theory (DFT) calculations and electron paramagnetic resonance (EPR) spectroscopy revealed the role of support in tuning the restructuring behaviors. Catalytic testing was further performed for phenylacetylene (PA) semi-hydrogenation and methane combustion reactions, and a reverse reactivity was achieved as a result of the different Pt restructuring behaviors on the two distinct TiO₂ supports.

Results

The crystal phase mediated redispersion/reshaping of Pt on anatase/rutile TiO₂

Approximately 1.0 nm Pt NPs were pre-synthesized using a modified literature approach³¹⁻³² with a uniform size distribution (Figure S1). The fresh Pt-TiO₂ catalysts were prepared by impregnation of pre-synthesized Pt NPs (0.5 wt.%) onto two commercially available anatase and rutile TiO₂ powders (see Table S1 and Figure S2). Figure S3 shows the X-ray powder diffraction (XRD) patterns, with a clear diffraction pattern for the TiO₂ support. No Pt diffraction peaks were observed due to their ultra-small particle sizes. Characterized by high-resolution TEM (HRTEM), the Pt NPs were uniformly dispersed on both the anatase and rutile TiO₂, and maintained their original particle sizes of 0.8–1.1 nm after impregnation. (See Figure 1a and b and Figure S5).

Subsequent calcination in the air up to 400°C resulted in the varied restructuring behavior of the Pt NPs on the two TiO₂ supports, as denoted by Pt/anatase-400 and Pt/rutile-400. The HRTEM images revealed that the Pt NPs become invisible on anatase TiO₂ after calcination (Figure 1a and b), suggesting the highly dispersed state of the Pt species in Pt/anatase-400. Using AC-STEM, we directly visualized the atomically dispersed isolated Pt SAs anchored on the anatase TiO₂ supports, due to the enhanced Z contrast in the high-angle annular dark-field (HAADF) images (Figure 1c). We also noted the coexistence of ultra-small Pt clusters of several atoms (see Figure 1c and S6), which may have required longer calcination or higher temperatures for complete atomic dispersion. By contrast, on rutile TiO₂, the calcination resulted in the reshaping of the Pt NPs, in the form of elongated particles, as shown in Figure 1e. The atomic resolved HAADF images (Figure 1f and Figure S7) further revealed a 2D planar shape of Pt/rutile-400 of 1-3 atomic layers thick. The edge-on particle in Figure 1f shows typical planar Pt NPs with two stacking layers of Pt (111), inferring the strong metal-support interactions^{6, 23, 33-34} that favored the wetting of Pt on the rutile TiO₂ interface^{6, 35-36} (more detailed evidence is shown in Supplementary Figure S7). CO chemisorption (Figure S8a) verified the same restructuring behavior in line with the (S)TEM results, where Pt/anatase-400 exhibited statistically higher dispersion and smaller particle sizes compared to Pt/rutile-400. FTIR spectra of CO adsorption on Pt/rutile-400 and Pt/anatase-400 (Figure 2a) were obtained to identify the nature of the different Pt species. Pt/rutile-400 presented both CO adsorption bands on the top (2076 cm⁻¹) and bridge sites (1850 cm⁻¹), which was characteristic for nanosized Pt particles, along with the 2106 cm⁻¹ band corresponding to CO adsorbed on the cationic Pt^{δ+} clusters.³⁷⁻³⁹ Pt/anatase-400, however, exhibited only linear CO stretching modes on the top sites. The lack of bridge-adsorption sites strongly indicated the ultra-small nature of Pt species on anatase TiO₂. Other than the linear CO adsorption on metallic Pt at 2076 cm⁻¹, the intensified peak at 2131 cm⁻¹ was ascribed to characteristic CO adsorption on Pt SAs due to the stronger interactions with surface oxygen^{14, 38} (see detailed peak assignments in Supplementary Discussion Section S4). Given the combined microscopic and spectroscopic results, we thus concluded the crystal phase-mediated restructuring of Pt/TiO₂ that anatase

phase favors atomically dispersed the Pt SAs along with a few ultra-small clusters (< 1 nm). By contrast, the rutile phase facilitated the reshaping of Pt NPs, forming 2D planar geometry.

Specific role of the support and underlying mechanisms for Pt restructuring

Surface defects are believed to play a significant role in stabilizing metal SAs.^{9, 37, 40-43} To characterize, we have performed the EPR experiments on both Pt-TiO₂ and pure TiO₂ supports after calcination, as shown in Figure 2b. A significantly enhanced EPR signal at $g = 1.982$ characteristic for Ti³⁺ was clearly identified on Pt/anatase-400 after calcination in the air, suggesting the preferential formation of Ti³⁺ defects as major anchoring sites for Pt SAs on anatase phase.⁴⁴⁻⁴⁷ This process is also promoted by the presence of Pt, since no Ti³⁺ signal was detected on pristine anatase TiO₂ after the same calcination procedure. (supplementary materials section S7) Thus, it can likely be rationalized by a reverse oxygen spillover from Ti⁴⁺ to Pt during calcination, forming Ti³⁺-O-Pt^{δ+} to stabilize ionic Pt atoms.⁴⁸ TPR (Figure S8b) and DFT calculations (Figure S9) were further performed to reveal support effect and the underlying mechanism. As shown in Figure S9, the oxygen atoms of anatase TiO₂(101) prefers to be trapped by Pt nanoparticles through reverse oxygen spillover mechanism involving a low kinetic barrier of 1.05 eV and forming Ti³⁺ defects.

In situ FTIR spectroscopy of CO adsorption on Pt/anatase during calcination is displayed in Figure S10. The IR frequency of linear CO adsorption on Pt gradually shifted from 2112 cm⁻¹ (CO on cationic Pt^{δ+} clusters) to 2139 cm⁻¹ (CO on isolated Pt atoms),¹⁴ reflecting the redispersion of Pt NPs/clusters into the SAs with increased calcination temperature. At ~350–400°C, a new band at 2186 cm⁻¹ emerged, which is characteristic for CO adsorption on as-formed Ti³⁺ sites during calcination.⁴⁹⁻⁵⁰ The Ti³⁺ defects on anatase TiO₂ thus facilitated the redispersion of Pt NPs by providing anchoring sites, which trapped single Pt atoms.¹⁰ This trapping mechanism was further validated by STEM-HAADF imaging of the Pt SAs on anatase TiO₂. As shown in Figure S11, most of the Pt SAs (92%) preferentially anchored on the Ti sites, suggesting superimposition on Ti³⁺ or Ti_{6c} substitution.¹¹ (see the Supplementary Discussion Section S1)

DFT calculations were conducted to understand the underlying mechanism for the crystal phase-mediated restructuring of the Pt/TiO₂ catalysts. The decomposition of metal particles and the migration of SAs (or small atomic clusters) from the larger particles were the two crucial steps for particle redispersion over the support surfaces via the reverse Ostwald Ripening process.⁵¹⁻⁵³ In this study, we employed a highly stable Pt₅₅ particle with an icosahedral (*I_h*) geometry and a diameter of ~1.03 nm,⁵⁴⁻⁵⁵ with a dominantly exposed (111) facet to model the Pt NPs according to the experimental results. As shown in Figure 2c, the rutile TiO₂(110) surface provided strong binding for Pt₅₅ with a binding energy (E_b) of -0.45 eV per Pt atom, which was higher than the anatase TiO₂(101) surface with $E_b = -0.23$ eV/atom. This was due to the fact that the oxygen atoms on the reconstructed rutile TiO₂(110) surface (Figure S12) captured more electrons (3.74 e) from Pt₅₅, according to the Bader charge analysis (Figure S13 and S14).⁵⁶ However, only 0.80 e from Pt₅₅ was transferred to the anatase

TiO₂(101) surface. Moreover, Pt₅₅ decomposed into Pt₅₄ and one Pt adatom (*Pt₅₅ → *Pt₅₄ + *Pt, shown in Figure 2c and S14) more easily on the anatase TiO₂ (101) surface with a kinetic barrier of 1.06 eV and reaction energy of 0.32 eV, than on the rutile TiO₂(110) surface (2.46 eV and 2.12 eV, respectively).

We further calculated the diffusion behavior of one Pt adatom on the surface of the two support types containing a Ti³⁺ defect. The anatase TiO₂(101) exhibits a smoother binding strength for Pt adatom corresponding adsorption energy with range of -2.34 ~ -3.13 eV than that of reconstructed rutile TiO₂(110) of -2.73 ~ 0.48 eV. (Figure S16 and S17) Figure 2d thus shows that the most stable sites of adsorbed Pt adatom is on the Ti³⁺ site of anatase TiO₂(101) with $E_b = -3.13$ eV, and on the bridge site with two O atoms for rutile TiO₂(110) with $E_b = -2.73$ eV, which is well consistent with previous report³⁸. However, the diffusion barrier of the Pt adatom on rutile TiO₂(110) was 3.21 eV, which was much higher than anatase TiO₂(101) (0.79 eV). This was due to the reconstructed oxygen on the rutile TiO₂(110), which formed a rough potential surface and hindered Pt diffusion.^{25, 53} Therefore, the Pt adatom was prone to diffusion and was further captured by the Ti³⁺ defects on anatase TiO₂(101), promoting reverse Ostwald Ripening. These results explained the experimental observations of the redispersion behavior of Pt on the anatase TiO₂. By contrast, the stronger binding of Pt₅₅ and the higher diffusion barrier of the Pt adatom on rutile TiO₂(110) confined the Pt NPs on the surface, and the wetting of the Pt NPs during calcination further resulted in a planar geometry as a result of the strong metal-support interactions.^{33, 35-36}

In situ STEM visualization of dynamic restructuring of Pt NPs on anatase/rutile TiO₂.

To directly visualize the dynamic redispersion of Pt on anatase TiO₂, in situ HAADF-STEM imaging was further employed in a 6 mbar O₂ environment from 100°C to 400°C, as shown in Figure 3a–d. To avoid the beam effect, the electron beam was shut off during heating (more detailed procedures and operations are listed in the Supplementary Discussion Section S1). As shown in Figure 3a, the pristine ~1 nm Pt NPs were stable up to 100°C in an O₂ environment. After heating up to 200°C, Pt was more mobile, likely due to the lower diffusion barrier on the anatase surface and the agglomeration of adjacent NPs, as indicated by a1, a2, and a4 (Figure 3a and b). At 300°C, the disappearance of the Pt NPs was observed, as marked by a1, a3, and a4, suggesting an onset of Pt redispersion. Meanwhile, the anatase-TiO₂ surface became more pitted, resulting in a growing number of dim patches due to the reduction of the anatase TiO₂ that formed at the same temperature range (see TPR in Figure S8b). The pitted structure thus provides undercoordinated step edges or defect sites that facilitates the trapping of Pt single atoms.⁵⁷⁻⁵⁹ Therefore, we established a strong correlation between the redispersion of Pt NPs and the formation of reduced Ti³⁺ defects. This was further evidenced by the a3 NP located on the defective area, which split into two smaller pieces at 200°C (Figure 3b) and eventually disappeared at 300°C (Figure 3). However, the a2 NP in the non-defective area remained integrated up to 400°C, and redispersion may require a longer calcination time or higher O₂ partial pressure.

For comparison, the dynamic evolution of the Pt NPs on rutile TiO₂ was visualized under identical in situ conditions. As shown in Figure 3e–h, most of the Pt NPs (r1 and r2) remained stable during calcination, while others (r3 and r4) slightly agglomerated until 300–400°C. This indicated that particle size slightly increased from 0.87 nm to 1.17 nm (see statistics in Figure S19). The stability of Pt NPs on the rutile surface thus suggested stronger support interactions and a higher diffusion barrier that confined the Pt NPs in position, which was in good agreement with our DFT calculations. Moreover, the rutile surface was less defective compared to anatase during the entire in situ experiment, which made the atomic dispersion of Pt more unfavorable.

Tunable reactivity of restructured Pt/TiO₂ mediated by the crystal phase of the support

The crystal phase mediated redispersion/reshaping of Pt/TiO₂ substantially influences their catalytic performance. Thus, two typical reactions, semi-hydrogenation of PA and methane combustion, were chosen as probe reactions to demonstrate the different catalytic reactivities of the Pt/anatase-400 (*Pt SAs*) and Pt/rutile-400 (*Pt planar NPs*) catalysts. Catalytic testing for semi-hydrogenation of PA to styrene (ST) was carried out in a batch reactor at 20°C (6 h), 30°C (4 h), and 50°C (1 h). As shown in Figure 4a, the isolated Pt SAs on anatase TiO₂ (Pt/anatase-400) exhibited high conversion and ST yields for all three testing conditions, resulting in ST yields of 65.0±6.7 % at 20°C for 6 h, 64.3±6.3 % at 30°C for 4 h, and 41.6±9.2 % at 50°C for 1 h. In comparison, the Pt planar NPs on rutile TiO₂ (Pt/rutile-400) showed only low activity with a PA conversion below 3.2% for all testing conditions. We thus confirmed that anatase-TiO₂ stabilized Pt SA catalysts were highly active for PA semi-hydrogenation rather than planar NPs for the rutile phase. This was likely attributed to the preferential -C≡C- activation and favorable diffusion of the *H species on single-atom Pt sites (Pt^{δ+}), despite the more favorable H₂ dissociation on Pt NPs.⁶⁰⁻⁶¹ The turn-over frequency (TOF) was further calculated which is among the highest reported values in literatures. (see Table S4 and supplementary discussion S6) For the methane combustion reaction (Figure 4b), Pt planar NPs on TiO₂ (Pt/rutile-400) exhibited nearly 100% CH₄ conversion at 400°C, which was remarkably higher than the isolated Pt atoms on anatase TiO₂ (Pt/anatase-400), which only had 18.2% conversion under the same conditions. We thus identified a reverse reactivity trend where rutile-TiO₂ stabilized Pt planar NPs exhibited better catalytic activity than Pt SAs on the anatase phase in terms of the methane combustion reaction. This was further rationalized by the preferential O₂ activation on Pt NPs over single atoms. The TOF was further calculated and comparable to the reported values in previous works. (see Table S5 and supplementary discussion S6)

To gain an atomistic insight, we systematically examined the dissociation of H₂ and O₂ molecules, and the binding strength of H and O atoms on Pt₁/anatase TiO₂(101) and Pt₅₅/rutile TiO₂(101) using DFT calculations (Figure S20, Table S2, and supplementary discussion section S3). Our results showed that the adsorbed H₂ molecules could dissociate into two H adatoms involving a low kinetic barrier ($E_a^{*H_2} < 0.48$ eV) for Pt₁/anatase TiO₂(101) and Pt₅₅/rutile TiO₂(110). Moreover, Pt₁/anatase TiO₂(101) provided moderate adsorption energy

of -0.10 eV for *H species (ΔE_{*H}), with the moderate binding of *H favoring the subsequent hydrogenation reaction. However, the binding of $\Delta E_{*H} = -1.21$ eV for Pt₅₅/rutile TiO₂(110) was too strong, which prevented the *H species from reacting. For O₂ dissociation, the O–O bond broke easily in Pt₅₅/rutile TiO₂(110) due to the kinetic barrier ($E_a^{*O_2}$) of 0.81 eV, which was beneficial for oxidation reaction; thus, the O₂ dissociation on Pt₁/anatase TiO₂(101) was much more difficult at $E_a^{*O_2} = 2.06$ eV. Therefore, this determined the tunable reactivity mediated by the different restructuring behaviors of the Pt catalysts on TiO₂, and Pt SAs favored the semi-hydrogenation reaction of PA, whereas stabilized Pt planar NPs promoted the oxidation reaction for methane (see Figure 4c). Our results thus provide a new route for precisely controlling the dynamic structure (size and shape) of Pt catalysts for designated reactions by simply choosing an appropriate support crystal phase.

Conclusion.

Two types of Pt/TiO₂ catalysts were prepared by impregnating as-synthesized Pt NPs (~1 nm) onto anatase and rutile TiO₂ supports. After calcination in the air at 400°C, a crystal phase mediated restructuring of Pt NPs on TiO₂ was clearly identified. (S)TEM imaging along with CO chemisorption and FTIR experiments provided solid evidence for the redispersion/reshaping of Pt NPs, indicating that rutile TiO₂ stabilized the Pt NPs with 2D planar geometry, whereas the anatase phase favored isolated Pt SAs. In situ STEM provided dynamic insight and real-time evidence for the dynamic restructuring of Pt on both anatase and rutile TiO₂. The reverse oxygen spillover very likely facilitates the stabilization of Pt SAs on anatase TiO₂ via promoted Ti³⁺ defects validated by EPR results. DFT calculations further revealed that the diffusion barrier of Pt adatom on rutile TiO₂(110) is 3.21 eV, much higher than that on anatase TiO₂(101) (0.79 eV). The anatase TiO₂(101) has a smooth potential energy surface, which is beneficial to diffusion of Pt adatom to forming atomically dispersed Pt catalysts.

The reactivities of the two catalysts, Pt/anatase-400 and Pt/rutile-400 were tested for two typical reactions: semi-hydrogenation of phenylacetylene and methane combustion. A reverse reactivity was achieved by tuning the dynamic behavior of Pt restructuring on the two different TiO₂ supports. Isolated Pt SAs on anatase TiO₂ (Pt/anatase-400) exhibited much higher conversion and styrene yields for the semi-hydrogenation of PA, while the Pt planar NPs on rutile (Pt/rutile-400) were remarkably active during methane oxidation.

In summary, we discovered and visualized the in situ restructuring (redispersion/reshaping) of Pt catalysts mediated by the crystal phases of TiO₂, as a simple approach for the fabrication and design of Pt catalyst with precise dispersion, shape, and reactivity control.

Methods

Chemicals and materials

All chemicals are commercially available and were used as received. Platinum (IV) acid (H₂PtCl₆·6H₂O, 40%), sodium borohydride (NaBH₄, 99.9%), ethanol (HPLC grade, 99.9%),

3-mercaptopropionic acid (HSC₂H₄COOH, 99%), and TiO₂ (rutile, anatase) were purchased from Adamas, while ultrapure water (resistance 18.2 MΩ·cm) was purified using a Barnstead NANO pure Diwater TM system. All glassware was thoroughly cleaned with aqua regia (HCl: HNO₃ = 3: 1, v/v), rinsed with copious amounts of ultrapure water, and then dried in an oven prior to use.

Sample preparation.

A modified literature approach for the synthesis of Pt NPs was used.³¹⁻³² In this work, H₂PtCl₆·6H₂O (0.1 mmol) was dissolved in 10 ml ethanol, then 3-mercaptopropionic acid (molar ratio of thiol/Pt: 6/1) was added to the solution, and the mixture was stirred for 20 min. An aqueous solution of NaBH₄ (0.3 mmol in 2 ml water) was then quickly added to reduce Pt (IV) to Pt (0). The reaction was allowed to proceed for one hour. After centrifugation (9000 rpm, 10 min), 1.9 g of TiO₂ powder (rutile and anatase) was added to the solution. After stirring for three hours at room temperature (RT), the supernatant became colorless, indicating that the Pt NPs were loaded onto the TiO₂ surface. Then the solid was collected by centrifugation and washed with ethanol three times. Afterward, the catalysts were dried at 100°C in open air. The Pt/TiO₂-400 (Pt/anatase-400 and Pt/rutile-400) were obtained after the calcination process at 400°C for four hours to activate the restructuring process.

Catalytic testing

Semi-hydrogenation of phenylacetylene. A 10 ml Schlenk flask was fitted with a balloon filled with H₂. The tube was charged with 20 mg of catalyst, 3 ml of ethanol, and 0.7 mmol of PA. Then the flask was flushed with H₂ and tightly sealed at a balloon pressure of H₂, and then stirred at 20°C for 6 h, 30°C for four hours, and 50°C for one hour. The products were analyzed by a 7820A gas chromatograph (GC) equipped with a flame ionization detector (FID) and a HP-5 capillary column. A known amount of n-octane was used as the internal standard. The conversion of PA (χ_{PA}) and the yield of expected product ST were determined by:

$$\chi_{PA}(\%) = \frac{PA_{\text{feed}}(\text{mol}) - PA_{\text{residue}}(\text{mol})}{PA_{\text{feed}}(\text{mol})} \times 100\% \quad \text{Equation (1)}$$

$$\text{Yield}_{\text{ST}}(\%) = \frac{ST_{\text{product}}(\text{mol})}{PA_{\text{feed}}(\text{mol})} \times 100\% \quad \text{Equation (2)}$$

$$r_{PA} = \frac{n_{PA} \times \chi_{PA}}{m_{\text{Cat}} \times w_{Pt} \times t} (\text{mol} \cdot \text{s}^{-1} \cdot \text{g}^{-1}) \quad \text{Equation (3)}$$

$$\text{TOF} = \frac{r_{PA} \times M_{Pt}}{D_{Pt}} (\text{s}^{-1}) \quad \text{Equation (4)}$$

Methane combustion. The catalytic testing was carried out in a fixed bed reactor at ambient pressure, where 100 mg of catalyst sample was induced in the middle of the reaction tube. Then, the reactant gas CH₄/O₂/He = 1/20/79 (v/v) was introduced into the reaction system at a rate of 60 ml/min. Catalyst evaluation was performed at 1°C intervals from 70°C

to 400°C, at a space velocity of 36,000 ml h⁻¹ g⁻¹. All the products from the reaction were in situ analyzed using a gas chromatograph system (Agilent 7890B) with a TDX-01 carbon molecular sieve column. The detectors consisted of a flame ionization detector (FID) and thermal conductivity detector (TCD). The CH₄ conversion (χ_{CH_4}) was determined by Equation (5). The kinetic measurements were performed with the methane conversion lower than 10% in order to eliminate the thermal and diffusion effects. The reaction rates (r_{CH_4}) and TOF were calculated by equation (6) and (7).

$$\chi_{CH_4} (\%) = \frac{C_{CH_4}^{In} - C_{CH_4}^{out}}{C_{CH_4}^{in}} \times 100\% \quad \text{Equation (5)}$$

$$r_{CH_4} = \frac{c_{CH_4} \times \chi_{CH_4} \times V \times p_{atm}}{m_{cat} \times w_{Pt} \times R \times T} \text{ (mol} \cdot \text{s}^{-1} \cdot \text{g}_{Pt}^{-1}\text{)} \quad \text{Equation (6)}$$

$$\text{TOF} = \frac{r_{CH_4} \times M_{Pt}}{D_{Pt}} \text{ (s}^{-1}\text{)} \quad \text{Equation (7)}$$

Characterizations

High-resolution TEM analysis was performed on JEM 2100 working at 200 kV. The STEM analysis and elemental mapping were performed on a JEM ARM200F thermal-field emission microscope with a probe Cs-corrector working at 200 kV. For the HAADF imaging, a convergence angle of ~23 mrad and collection angle range of 68–174 mrad were adapted for the incoherent atomic number imaging. The elemental composition as well as distribution were analyzed with an energy dispersive X-ray analyzer (EDS, EX-230 100m² detector) equipped on the microscope.

In situ STEM experiments were carried out on the Themis ETEM (Thermo Scientific Company), equipped with 300 kV Schottky emission gun and Cs corrector for parallel imaging (CEOS GmbH). The sample (Pt/anatase-fresh and Pt/rutile-fresh) was loaded on a Si₃N₄ membrane and heated in situ using a micro-electromechanical system (MEMS) based heating method (FEI NanoEX). The in situ experiments were imitated at 100°C under ultra-high vacuum (UHV) conditions to exclude carbon contamination and then collected the HAADF/BF images simultaneously in an environment of 6.0±0.1 mbar O₂ with increasing calcination temperatures. To minimize the electron beam effect, we shut off the beam during heating process and adopted other procedures (see Supplementary Discussion S2).

For *CO probed FTIR* characterization, all of the FTIR spectra were acquired in transmission mode scanning in range of 1000 cm⁻¹ and 4000 cm⁻¹ at 32-scans integral using a Bruker TENSOR27 spectrometer that was equipped with a mercury cadmium telluride (MCT) detector facilitating a resolution of 4 cm⁻¹. For CO-FTIR experiments, we first purged the cell with N₂ (50 ml/min) and collected a spectrum as the background. Then, we introduced CO (10 ml/min) and maintained the concentration for 10 min to reach saturation of CO on the Pt catalysts. Afterward, we evacuated CO by purging with N₂ (50 ml/min) and collected the FTIR spectra.

CO chemisorption was measured with a Micromeritics AutoChem 2920 II equipped with a thermal conductivity detector (TCD). The data were analyzed using the software of MicroActive for AutoChem II 2920 Version 6.01.

For *temperature programmed reduction (TPR)*, H₂-TPR was performed on a Micromeritics AutoChem 2920 II instrument. The experiments were performed in a fix bed U-tube reactor using a mixture of 5% H₂/Ar gas at a flow rate of 30 ml/min, with a heating rate of 10°C/min from room temperature to 600°C. The amount of H₂ consumption was analyzed with a TCD detector.

X-ray diffraction (XRD) patterns were collected using a PAN analytical X'Pert Pro diffractometer equipped with graphite monochromator and Cu Ka radiation (40 kV and 30 mA). The data were analyzed using HighScorePlus 4.8.0 software.

The Electron Paramagnetic Resonance (EPR) spectra were recorded at 100 K using a Bruker A200 EPR spectrometer. All spectra were collected under the same experimental conditions with the following EPR parameter settings: microwave frequency, 9.30 GHz; center field, 3330 G; sweep width, 600 G; modulation frequency, 100 kHz; and power, 10.00 mW.

Theoretical calculations.

All theoretical calculations were carried by applying the density functional theory. See detailed information in the Supplementary Methods.

Data availability.

All data needed to support the plots and evaluate the conclusions within this paper are present in the paper and the supplementary materials.

References

1. Liu, L.; Corma, A., Metal Catalysts for Heterogeneous Catalysis: From Single Atoms to Nanoclusters and Nanoparticles. *Chem. Rev.* **118**, 4981-5079 (2018).
2. Xie, C., et al., Surface and Interface Control in Nanoparticle Catalysis. *Chem. Rev.* **120**, 1184-1249 (2020).
3. Jeong, H., et al., Highly durable metal ensemble catalysts with full dispersion for automotive applications beyond single-atom catalysts. *Nat. Catal.* **3**, 368-375 (2020).
4. Shi, X., et al., Copper Catalysts in Semihydrogenation of Acetylene: From Single Atoms to Nanoparticles. *ACS Catal.* **10**, 3495-3504 (2020).
5. An, N., et al., Size Effects of Platinum Colloid Particles on the Structure and CO Oxidation Properties of Supported Pt/Fe₂O₃ Catalysts. *J. Phys. Chem. C* **117**, 21254-21262 (2013).
6. Schweitzer, N. M., et al., High Activity Carbide Supported Catalysts for Water Gas Shift. *J. Am. Chem. Soc.* **133**, 2378-2381 (2011).

7. Faur Ghenciu, A., Review of fuel processing catalysts for hydrogen production in PEM fuel cell systems. *Curr. Opin. Solid State Mater. Sci.* **6**, 389-399 (2002).
8. Qiao, B., et al., Single-atom catalysis of CO oxidation using Pt₁/FeO_x. *Nat. Chem.* **3**, 634 (2011).
9. Bulushev, D. A., et al., Single Atoms of Pt-Group Metals Stabilized by N-Doped Carbon Nanofibers for Efficient Hydrogen Production from Formic Acid. *ACS Catal.* **6**, 3442-3451 (2016).
10. Jones, J., et al., Thermally stable single-atom platinum-on-ceria catalysts via atom trapping. *Science* **353**, 150-154 (2016).
11. DeRita, L., et al., Structural evolution of atomically dispersed Pt catalysts dictates reactivity. *Nat. Mater.* **18**, 746-751 (2019).
12. Kuai, L., et al., Titania supported synergistic palladium single atoms and nanoparticles for room temperature ketone and aldehydes hydrogenation. *Nat. Commun.* **11**, 48-57 (2020).
13. Moliner, M., et al., Reversible Transformation of Pt Nanoparticles into Single Atoms inside High-Silica Chabazite Zeolite. *J. Am. Chem. Soc.* **138**, 15743-15750 (2016).
14. Ding, K., et al., Identification of active sites in CO oxidation and water-gas shift over supported Pt catalysts. *Science* **350**, 189-192 (2015).
15. He, Q., et al., Population and hierarchy of active species in gold iron oxide catalysts for carbon monoxide oxidation. *Nat. Commun.* **7**, 12905 (2016).
16. Maurer, F., et al., Tracking the formation, fate and consequence for catalytic activity of Pt single sites on CeO₂. *Nat. Catal.* **3**, 824-833 (2020).
17. Zhang, X., et al., Reversible loss of core-shell structure for Ni-Au bimetallic nanoparticles during CO₂ hydrogenation. *Nat. Catal.* **3**, 411-417 (2020).
18. Zhu, B., et al., Reshaping of Metal Nanoparticles Under Reaction Conditions. *Angew. Chem. Int. Ed.* **59**, 2171-2180 (2020).
19. Wei, S., et al., Direct observation of noble metal nanoparticles transforming to thermally stable single atoms. *Nat. Nanotechnol.* **13**, 856-861 (2018).
20. Lang, R., et al., Non defect-stabilized thermally stable single-atom catalyst. *Nat. Commun.* **10**, 234-243 (2019).
21. Chee, S. W., et al., Structural changes in noble metal nanoparticles during CO oxidation and their impact on catalyst activity. *Nat. Commun.* **11**, 2133 (2020).

22. Tang, M., et al., Recent Progresses on Structural Reconstruction of Nanosized Metal Catalysts via Controlled-Atmosphere Transmission Electron Microscopy: A Review. *ACS Catal.* **10**, 14419-14450 (2020).
23. Dong, J., et al., Carbide-Supported Au Catalysts for Water–Gas Shift Reactions: A New Territory for the Strong Metal–Support Interaction Effect. *J. Am. Chem. Soc.* **140**, 13808-13816 (2018).
24. Yang, B., et al., Stabilizing Gold Adatoms by Thiophenyl Derivatives: A Possible Route toward Metal Redispersion. *J. Am. Chem. Soc.* **134**, 11161-11167 (2012).
25. Ouyang, R., et al., Atomistic Theory of Ostwald Ripening and Disintegration of Supported Metal Particles under Reaction Conditions. *J. Am. Chem. Soc.* **135**, 1760-1771 (2013).
26. Lang, R., et al., Single-Atom Catalysts Based on the Metal–Oxide Interaction. *Chem. Rev.* **120**, 11986-12043 (2020).
27. Han, B., et al., Strong Metal-Support Interactions between Pt Single Atoms and TiO₂. *Angew. Chem. Int. Ed.* **59**, 11824-11829 (2020).
28. Tauster, S. J., et al., Strong metal-support interactions. Group 8 noble metals supported on titanium dioxide. *J. Am. Chem. Soc.* **100**, 170-175 (1978).
29. Tauster, S. J., Strong metal-support interactions. *Acc. Chem. Res.* **20**, 389-394 (1987).
30. Chen, A., et al., Structure of the catalytically active copper-ceria interfacial perimeter. *Nat. Catal.* **2**, 334-341 (2019).
31. Wu, Z., et al., One-pot synthesis of atomically monodisperse, thiol-functionalized Au₂₅ nanoclusters. *J. Mater. Chem.* **19**, 622-626 (2009).
32. Eklund, S. E.; Cliffler, D. E., Synthesis and Catalytic Properties of Soluble Platinum Nanoparticles Protected by a Thiol Monolayer. *Langmuir* **20**, 6012-6018 (2004).
33. Chen, A., et al., Structure of the catalytically active copper–ceria interfacial perimeter. *Nat. Catal.* **2**, 334-341 (2019).
34. Ma, Y., et al., Embedded structure catalyst: a new perspective from noble metal supported on molybdenum carbide. *RSC Adv.* **5**, 15002-15005 (2015).
35. Hansen, P. L., et al., Atom-Resolved Imaging of Dynamic Shape Changes in Supported Copper Nanocrystals. *Science* **295**, 2053-2055 (2002).
36. Chen, M. S.; Goodman, D. W., The Structure of Catalytically Active Gold on Titania. *Science* **306**, 252-255 (2004).
37. DeRita, L., et al., Catalyst Architecture for Stable Single Atom Dispersion Enables Site-Specific Spectroscopic and Reactivity Measurements of CO Adsorbed to Pt Atoms,

- Oxidized Pt Clusters, and Metallic Pt Clusters on TiO₂. *J. Am. Chem. Soc.* **139**, 14150-14165 (2017).
38. Thang, H. V., et al., Nature of stable single atom Pt catalysts dispersed on anatase TiO₂. *J. Catal.* **367**, 104-114 (2018).
39. Zhu Chen, J., et al., Identification of the structure of the Bi promoted Pt non-oxidative coupling of methane catalyst: a nanoscale Pt₃Bi intermetallic alloy. *Catal. Sci. Technol.* **9**, 1349-1356 (2019).
40. Abbet, S., et al., Acetylene Cyclotrimerization on Supported Size-Selected Pd_n Clusters (1 ≤ n ≤ 30): One Atom Is Enough! *J. Am. Chem. Soc.* **122**, 3453-3457 (2000).
41. Kwak, J. H., et al., Coordinatively Unsaturated Al³⁺ Centers as Binding Sites for Active Catalyst Phases of Platinum on γ-Al₂O₃. *Science* **325**, 1670-1673 (2009).
42. Sasahara, A., et al., Probe Microscope Observation of Platinum Atoms Deposited on the TiO₂(110)-(1 × 1) Surface. *J. Phys. Chem. B* **110**, 13453-13457 (2006).
43. Hejazi, S., et al., On the Controlled Loading of Single Platinum Atoms as a Co-Catalyst on TiO₂ Anatase for Optimized Photocatalytic H₂ Generation. *Adv. Mater.* **32**, 1908505 (2020).
44. Li, G., et al., The Important Role of Tetrahedral Ti⁴⁺ Sites in the Phase Transformation and Photocatalytic Activity of TiO₂ Nanocomposites. *J. Am. Chem. Soc.* **130**, 5402-5403 (2008).
45. Zuo, F., et al., Self-Doped Ti³⁺ Enhanced Photocatalyst for Hydrogen Production under Visible Light. *J. Am. Chem. Soc.* **132**, 11856-11857 (2010).
46. Khomenko, V. M., et al., Electronic absorption by Ti³⁺ ions and electron delocalization in synthetic blue rutile. *Phys. Chem. Miner.* **25**, 338-346 (1998).
47. Anpo, M., et al., Generation of superoxide ions at oxide surfaces. *Top. Catal.* **8**, 189 (1999).
48. Muravev, V., et al., Interface dynamics of Pd–CeO₂ single-atom catalysts during CO oxidation. *Nat. Catal.* **4**, 469-478 (2021).
49. Fernandez, A., et al., Spectroscopic characterization of TiO₂/SiO₂ catalysts. *J. Catal.* **112**, 489-494 (1988).
50. Li, Y., et al., The effect of titania polymorph on the strong metal-support interaction of Pd/TiO₂ catalysts and their application in the liquid phase selective hydrogenation of long chain alkadienes. *J. Mol. Catal. A: Chem.* **216**, 107-114 (2004).
51. Hansen, T. W., et al., Sintering of Catalytic Nanoparticles: Particle Migration or Ostwald Ripening? *Acc. Chem. Res.* **46**, 1720-1730 (2013).

52. Campbell, C. T., The Energetics of Supported Metal Nanoparticles: Relationships to Sintering Rates and Catalytic Activity. *Acc. Chem. Res.* **46**, 1712-1719 (2013).
53. Yuan, W., et al., Direct In Situ TEM Visualization and Insight into the Facet-Dependent Sintering Behaviors of Gold on TiO₂. *Angew. Chem. Int. Ed.* **57**, 16827-16831 (2018).
54. Xiao, L.; Wang, L., Structures of Platinum Clusters: Planar or Spherical? *J. Phys. Chem. A* **108**, 8605-8614 (2004).
55. Okamoto, Y., Density-functional calculations of atomic and molecular adsorptions on 55-atom metal clusters: Comparison with (111) surfaces. *Chem. Phys. Lett.* **405**, 79-83 (2005).
56. Henkelman, G., et al., A fast and robust algorithm for Bader decomposition of charge density. *Comp. Mater. Sci.* **36**, 354-360 (2006).
57. Jiang, D., et al., Tailoring the Local Environment of Platinum in Single-Atom Pt1/CeO₂ Catalysts for Robust Low-Temperature CO Oxidation. *Angew. Chem. Int. Ed.* <https://doi.org/10.1002/anie.202108585>, (2021).
58. Dvořák, F., et al., Creating single-atom Pt-ceria catalysts by surface step decoration. *Nat. Commun.* **7**, 10801 (2016).
59. Wang, H., et al., Surpassing the single-atom catalytic activity limit through paired Pt-O-Pt ensemble built from isolated Pt1 atoms. *Nat. Commun.* **10**, 3808 (2019).
60. Li, C., et al., Carbon nanotubes supported Pt catalysts for phenylacetylene hydrogenation: effects of oxygen containing surface groups on Pt dispersion and catalytic performance. *Catal. Today* **186**, 69-75 (2012).
61. Liang, H., et al., Porous TiO₂/Pt/TiO₂ Sandwich Catalyst for Highly Selective Semihydrogenation of Alkyne to Olefin. *ACS Catal.* **7**, 6567-6572 (2017).

Acknowledgments

This work received financial support from the National Natural Science Foundation of China (NO. 21872145, 22072151, 91961204), CAS Project for Young Scientists in Basic Research (YSBR-022) and Dalian Institute of Chemical Physics (DICP I202107). G.L. acknowledges the Liaoning Revitalization Talents Program (No. XLYC1807121). We specially thank Mengmeng Wang for assistance with catalytic testing, Qike Jiang and Yang Zhao for assistance with STEM and TEM characterization, Hiroaki Matsumoto and Chaobin Zeng (Hitachi High-Technologies) for assistance with the in situ STEM characterization, and Prof. Zhaochi Feng for assistance with the Raman experiments.

Author contributions

The project was conceived by B.Y. and G.L.. X.Z. performed TEM, partial FTIR, CO chemisorption, EPR characterizations and partial catalytic performance testing as well as the

data analysis under the supervision of B.Y.. Z.L. performed the catalyst preparation, partial FTIR, TPR characterizations and partial catalytic performance testing under the supervision of G.L. and W. S.. W.P., S.Z. and J.Z. conducted mechanism analysis via DFT calculations. W.L. performed partial STEM experiments. P.D., Z.W. and Z.Q. participated partial experiments and assisted the data analysis. J.Z. and W.S. provided the guidance and the funding support. All authors participated the manuscript written and revision.

Competing interests

The authors declare no competing interests.

Figures:

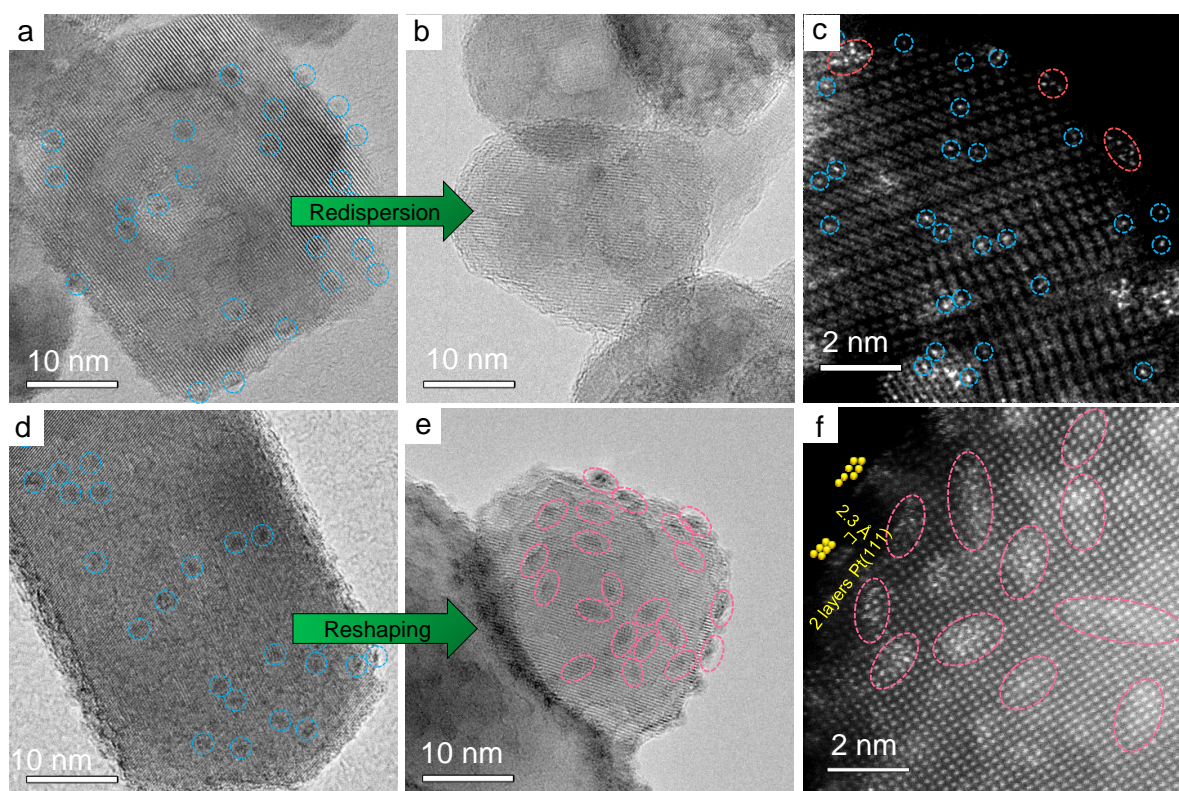


Fig. 1 | Direct visualization of the crystal phase mediated by redispersion/reshaping of Pt on anatase/rutile TiO₂. TEM (a, b, d, and e) and AC-STEM (c, f) images of Pt restructuring on anatase and rutile TiO₂ before and after calcination, (a) Pt/anatase-fresh; (b and c) Pt/anatase-400, (d) Pt/rutile-fresh; and (e and f) Pt/rutile-400. The inserted schematic showed the typical edge-on Pt NPs of planar shape with two stacking layers of Pt(111). The green arrows show the evolution of two Pt/TiO₂ samples after 400 °C calcination in air for 4 hours.

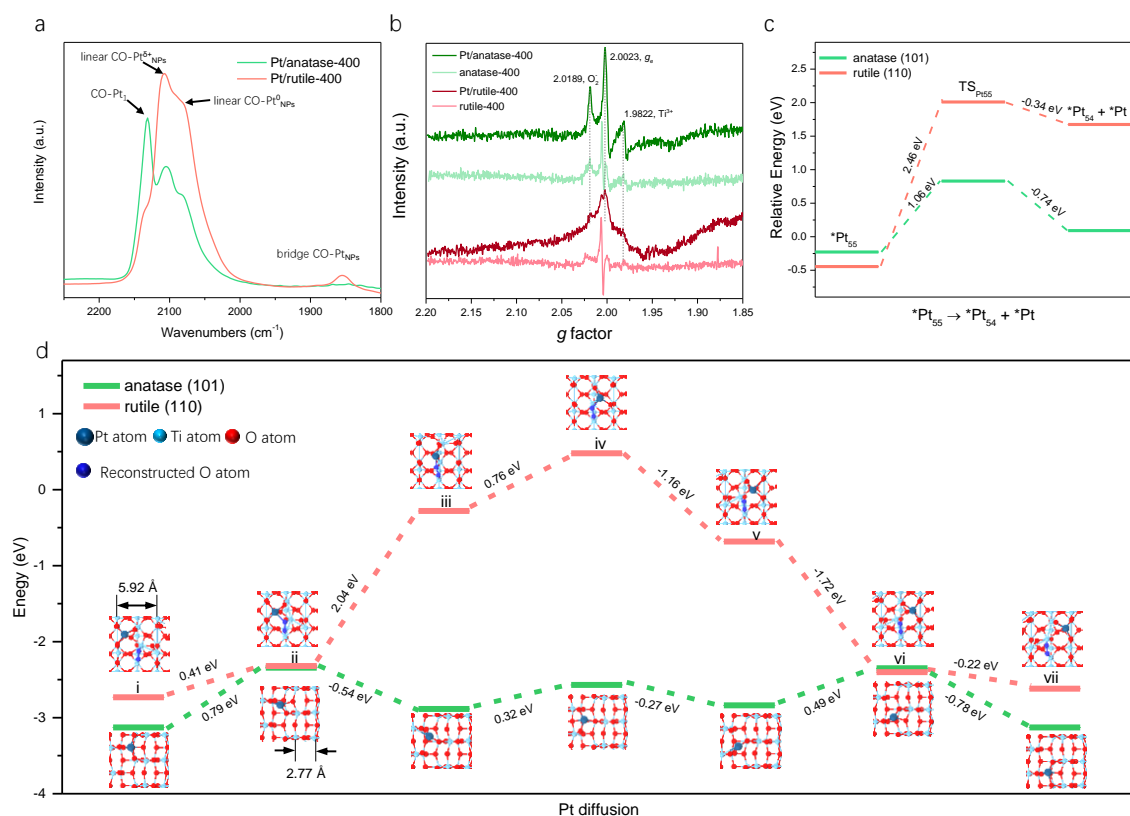


Fig. 2 | Spectroscopic characterization and mechanism studies for the restructuring of Pt/TiO₂ catalysts. (a) FTIR spectra of CO adsorption upon Pt/anatase-400 (green line) and Pt/rutile-400 (red line), (b) EPR spectra record at 100K of pure TiO₂ and Pt/TiO₂ samples after calcination (denoted as anatase-400, rutile-400 and Pt/anatase-400, Pt/rutile-400), (c) reaction pathway for the decomposition of Pt₅₅ to Pt₅₄ and one Pt adatom ($*Pt_{55} \rightarrow *Pt_{54} + *Pt$) on the anatase TiO₂(101) and rutile TiO₂(110) surface, and (d) DFT calculations for the diffusion of the Pt atom on anatase (green line) and rutile (red line).

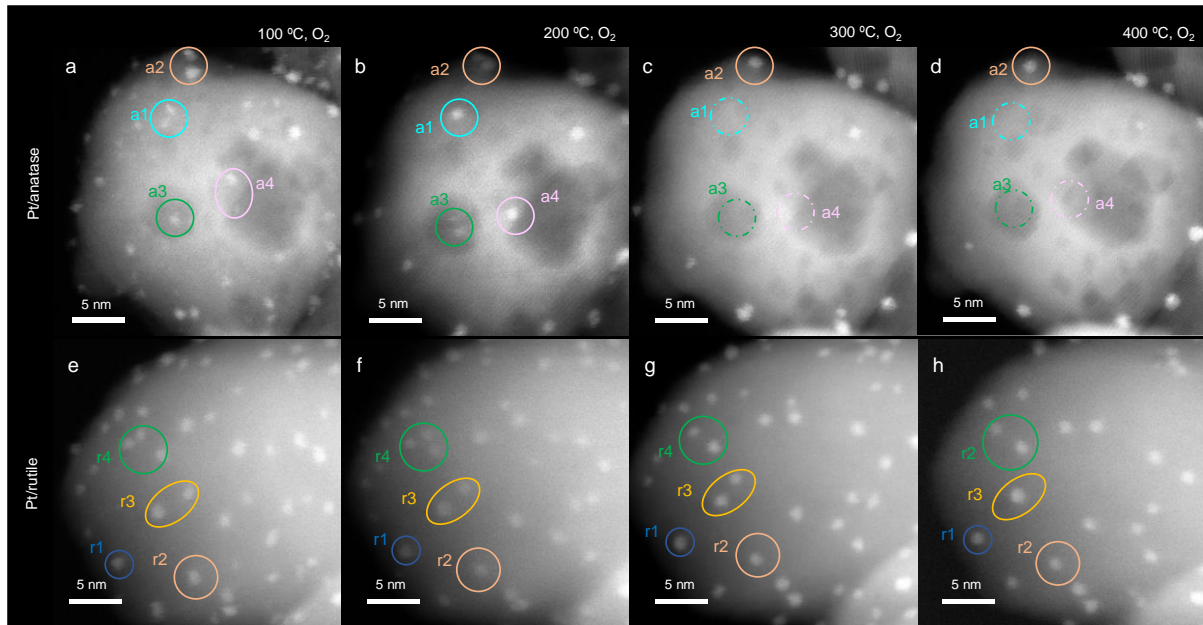


Fig. 3 | In situ STEM observation of dynamic restructuring of Pt NPs on anatase/rutile TiO_2 . (a-d) structural evolution of Pt on anatase TiO_2 , (a) 100 °C; (b) 200 °C; (c) 300 °C; (d) 400 °C; (e-h) structural evolution of Pt on rutile TiO_2 , (e) 100 °C; (f) 200 °C; (g) 300 °C; (h) 400 °C. In situ experiments were conducted in a 6 mbar O_2 environment. All scale bar is 5 nm.

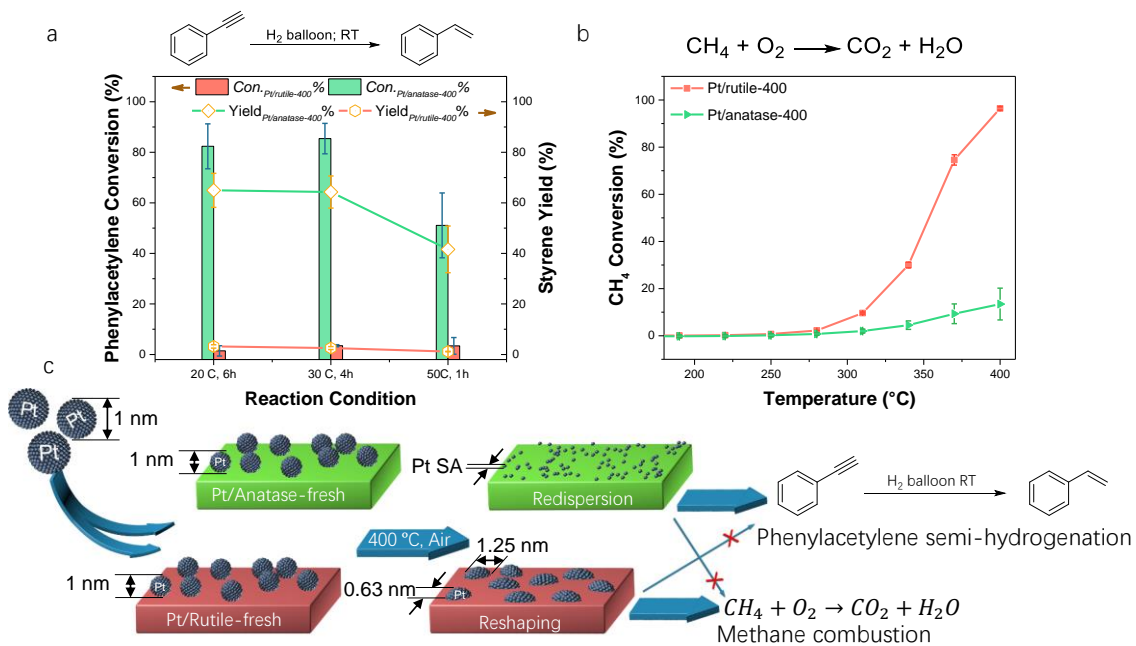


Fig. 4 | Reactivity and scheme of crystal phase mediated by Pt restructuring on TiO₂. Catalytic performance of Pt/anatase-400 (red line) and Pt/rutile-400 (green line) catalysts, (a) PA semi-hydrogenation reaction and (b) methane combustion reaction, and (c) scheme of the crystal phase-mediated restructuring and reactivity of Pt/TiO₂.

Table of Contents

